

EMPIRICAL MODELS FOR DARK MATTER HALOS. I. NONPARAMETRIC CONSTRUCTION OF DENSITY PROFILES AND COMPARISON WITH PARAMETRIC MODELS

DAVID MERRITT

Department of Physics, Rochester Institute of Technology, Rochester, NY 14623

ALISTER W. GRAHAM¹

Mount Stromlo and Siding Spring Observatories, Australian National University, Weston Creek, ACT 2611, Australia

BEN MOORE

University of Zurich, CH-8057 Zurich, Switzerland

JÜRIG DIEMAND

Department of Astronomy and Astrophysics, University of California, Santa Cruz, CA 95064

AND

BALŠA TERZIĆ

Department of Physics, Northern Illinois University, DeKalb, IL 60115

Received 2006 May 11; accepted 2006 September 1

ABSTRACT

We use techniques from nonparametric function estimation theory to extract the density profiles, and their derivatives, from a set of N -body dark matter halos. We consider halos generated from Λ CDM simulations of gravitational clustering, as well as isolated spherical collapses. The logarithmic density slopes $\gamma \equiv d \log \rho / d \log r$ of the Λ CDM halos are found to vary as power laws in radius, reaching values of $\gamma \approx -1$ at the innermost resolved radii, $\sim 10^{-2} r_{\text{vir}}$. This behavior is significantly different from that of broken-power-law models like the Navarro-Frenk-White (NFW) profile but similar to that of models like de Vaucouleurs's. Accordingly, we compare the N -body density profiles with various parametric models to find which provide the best fit. We consider an NFW-like model with arbitrary inner slope; Dehnen & McLaughlin's anisotropic model; Einasto's model (identical in functional form to Sérsic's model but fitted to the space density); and the density model of Prugniel & Simien that was designed to match the deprojected form of Sérsic's $R^{1/n}$ law. Overall, the best-fitting model to the Λ CDM halos is Einasto's, although the Prugniel-Simien and Dehnen-McLaughlin models also perform well. With regard to the spherical-collapse halos, both the Prugniel-Simien and Einasto models describe the density profiles well, with an rms scatter some 4 times smaller than that obtained with either the NFW-like model or the three-parameter Dehnen-McLaughlin model. Finally, we confirm recent claims of a systematic variation in profile shape with halo mass.

Key words: dark matter — galaxies: halos — methods: n -body simulations

1. INTRODUCTION

A fundamental question is the distribution of matter in bound systems (galaxies, galaxy clusters, and dark matter halos) that form in an expanding universe. Early work on the self-similar collapse of (spherical) primordial overdensities resulted in virialized structures having density profiles described by a single power law (e.g., Fillmore & Goldreich 1984; Bertschinger 1985; Hoffman 1988). Some of the first N -body simulations were simple cold-collapse calculations like these (e.g., van Albada 1961; Aarseth 1963; Hénon 1964; Peebles 1970). It was quickly realized that given appropriately low but nonzero levels of initial random velocity, the end state of such systems departed from a simple power law, resembling instead the de Vaucouleurs (1948) $R^{1/4}$ profiles observed in elliptical galaxies (e.g., van Albada 1982; Aguilar & Merritt 1990). A closer reinspection of the data, however (e.g., Figs. 4–6 in van Albada 1982; Fig. 4 in Carlberg et al. 1986) reveals obvious and systematic deviations from the $R^{1/4}$ model in the cold collapses (see also Nipoti et al. 2006). From a visual inspection of these figures, one can see that the distributions would be better described with an $R^{1/n}$ profile with $n < 4$.

As N -body techniques improved, the logarithmic profile slopes of cold dark matter (CDM) halos, simulated in hierarchical merger models, were also observed to steepen with increasing radius (e.g., West et al. 1987; Frenk et al. 1988; Efstathiou et al. 1988). Dubinski & Carlberg (1991) adopted Hernquist's (1990) double-power-law model (itself a modification of Jaffe's [1983] model) to describe these density profiles. This empirical model has an inner logarithmic slope of -1 and an outer logarithmic slope of -4 . It was introduced as an analytical approximation to the deprojected form of de Vaucouleurs' (1948) profile. Navarro et al. (1995) modified this to give the so-called Navarro-Frenk-White (NFW) model, which has an outer logarithmic slope of -3 rather than -4 , while Moore et al. (1998, 1999) suggested that a further variation having an inner logarithmic slope of -1.4 or -1.5 might be more appropriate.

The density profiles of N -body halos typically span only ~ 2 decades in radius, between the virial radius and an inner limit set by the N -body resolution. It has long been clear that other functional forms might fit such limited data as well or better than the NFW or Moore profiles. Recently, Navarro et al. (2004) argued for a model, like de Vaucouleurs's in which the logarithmic slope varies continuously with radius:

$$\frac{d \ln \rho}{d \ln r} = -2 \left(\frac{r}{r-2} \right)^\alpha, \quad (1)$$

¹ Current address: Centre for Astrophysics and Supercomputing, Swinburne University of Technology, Hawthorn, VIC 3122, Australia.

i.e.,

$$\rho(r) \propto \exp(-Ar^\alpha), \quad (2)$$

where r_{-2} is the radius at which the logarithmic slope of the density is -2 and α is a parameter describing the degree of curvature of the profile. Merritt et al. (2005) pointed out that this is the same relation between slope and radius that defines Sérsic's (1963, 1968) model, with the difference that Sérsic's model is traditionally applied to the projected (surface) densities of galaxies, not to the space density. Merritt et al. further showed that the (space) density profiles of a sample of N -body halos were equally well fitted by equation (2) or by a deprojected Sérsic profile, and that both of these models provide better fits than an NFW-like, double-power-law model with a variable inner slope. Hence, Sérsic's model—the function that is so successful at describing the luminosity profiles of early-type galaxies and bulges (e.g., Caon et al. 1993; Graham & Guzmán 2003; and references therein) and the projected density of hot gas in galaxy clusters (Demarco et al. 2003)—is also an excellent description of N -body halos.

(To limit confusion, we henceforth refer to eq. [2] as “Einasto's $r^{1/n}$ model” when applied to space density profiles and as “Sérsic's $R^{1/n}$ model” when applied to projected density profiles, with R the radius on the plane of the sky. The former name acknowledges Einasto's [1965, 1968, 1969] early and extensive use of eq. [2] to model the light and mass distributions of galaxies [see also Einasto & Haud 1989]. In addition, we henceforth replace the exponent α by $1/n$ in keeping with the usage established by Sérsic and de Vaucouleurs.)

In this paper we continue the analysis of alternatives to the NFW and Moore profiles, using a new set of N -body halos. Among the various models that we consider is the Prugniel-Simien (Prugniel & Simien 1997) law, first developed as an analytic approximation to the deprojected form of the Sérsic $R^{1/n}$ profile. Apart from the work of Lima Neto et al. (1999), Pignatelli & Galletta (1999), and Márquez et al. (2000, 2001), the Prugniel-Simien model has received little attention to date. Demarco et al. (2003) have, however, applied it to the gas density profiles of 24 galaxy clusters observed with *ROSAT*, and Terzić & Graham (2005) showed that it provides a superior description of the density profiles of real elliptical galaxies compared with either the Jaffe or Hernquist models. As far as we are aware, ours is the first application of the Prugniel-Simien model to N -body halos.

As in Merritt et al. (2005), we base our model evaluations on *nonparametric* representations of the N -body density profiles. Such representations are “optimum” in terms of their bias-variance tradeoff but are also notable for their flexibility. Not only do they (1) constitute “stand-alone,” smooth, and continuous representations of the density and its slope, they are also well suited to (2) inferring best-fit values for the fitting parameters of parametric functions and (3) comparing the goodness of fit of different parametric models via the relative values of the integrated square error or a similar statistic. The more standard technique of computing binned densities is suitable (although inferior) for (2) and (3) but not for (1), since the density is given only at a discrete set of points and the derivatives are poorly defined, while techniques like Sarazin's (1980) maximum likelihood algorithm provide a (perhaps) more direct route to (2) but are not appropriate for (1) or (3). Recently, nonparametric function estimation methods have been applied to many other problems in astrophysics, including reconstruction of the cosmic microwave background fluctuation spectrum (Miller et al. 2002), dynamics of dwarf galaxies (Wang et al. 2005), and reconstruction of dark matter distributions via gravitational lensing (Abdelsalam et al. 1998). Application of

nonparametric methods to the halo density profile problem is perhaps overdue, especially given the importance of determining the inner density slope (Diemand et al. 2005).

In § 2 we introduce the data sets to be analyzed. These consist of N -body simulations of 10 Λ CDM halos and two halos formed by monolithic (nearly spherical) collapse. (Moore et al. [1999] have discussed the similarity between the end state of cold-collapse simulations and hierarchical CDM models.) In § 3 we present the nonparametric method used to construct the density profiles and their logarithmic slopes. Section 4 presents four different three-parameter models, and § 5 reports how well these empirical models perform. Our findings are summarized in § 7.

In Paper II of this series (Graham et al. 2006a) we explore the Einasto and Prugniel-Simien models in more detail. Specifically, we explore the logarithmic slope of these models and compare the results with observations of real galaxies. We also present the models' circular velocity profiles and their ρ/σ^3 profiles. Helpful expressions for the concentration and assorted scale radii (r_s , r_{-2} , r_e , R_e , r_{vir} , and r_{max} , the radius where the circular velocity profile has its maximum value) are also derived. Because the Prugniel-Simien model yields the same parameters as those coming from Sérsic-model fits, we are able to show in Paper III (Graham et al. 2006b) the location of our dark matter halos on the Kormendy diagram (μ_e vs. $\log R_e$), along with real galaxies. In addition, we show in Paper III the location of our dark matter halos and real galaxies and clusters in a new $\log(\rho_e)$ – $\log(R_e)$ diagram.

2. DATA: DARK MATTER HALOS

We use a sample of relaxed, dark matter halos from Diemand et al. (2004a, 2004b). Details about the simulations, convergence tests, and an estimate of the converged scales can be found in those papers. Briefly, the sample consists of six cluster-sized halos (models A09, B09, C09, D12, E09, and F09) resolved with 5–25 million particles within the virial radius, and four galaxy-sized halos (models G00, G01, G02, and G03) resolved with 2–4 million particles. The innermost resolved radii are 0.3%–0.8% of the virial radius, r_{vir} . The outermost data point is roughly at the virial radius, which is defined in such a way that the mean density within r_{vir} is $178\Omega_M^{0.45}\rho_{\text{crit}} = 98.4\rho_{\text{crit}}$ (Eke et al. 1996) using $\Omega_m = 0.268$ (Spergel et al. 2003). The virial radius thus encloses an overdensity that is 368 times denser than the mean matter density. We adopted the same estimates of the halo centers as in the Diemand et al. papers; these were computed using SKID (Stadel 2001), a kernel-based routine.

In an effort to study the similarities between cold, collisionless collapse halos and CDM halos, we performed two additional simulations. We distributed 10^7 particles with an initial density profile $\rho(r) \propto r^{-1}$, within a unit radius sphere with total mass 1 (M11) and 0.1 (M35). The particles were given zero kinetic energy, and the gravitational softening was set to 0.001. Each system collapsed and experienced a radial-orbit instability (Merritt & Aguilar 1985) that resulted in a virialized, triaxial/prolate structure. The lower mass halo, M35, collapsed less violently over a longer period of time.

3. NONPARAMETRIC ESTIMATION OF DENSITY PROFILES AND THEIR DERIVATIVES

Density profiles of N -body halos are commonly constructed by counting particles in bins. While a binned histogram is a bona fide nonparametric estimate of the “true” density profile, it has many undesirable properties; e.g., it is discontinuous, and it depends sensitively on the chosen size and location of the bins (see, e.g., Stepanas & Saha 1995). A better approach is to view the

particle positions as a random sample drawn from some unknown, smooth density $\rho(\mathbf{r})$, and to use techniques from nonparametric function estimation to construct an estimate $\hat{\rho}$ of ρ (e.g., Scott 1992). In the limit that the “sample size” N tends to infinity, such an estimate exactly reproduces the density function from which the data were drawn, as well as many properties of that function, e.g., its derivatives (Silverman 1986).

We used a kernel-based algorithm for estimating $\rho(r)$, similar to the algorithms described in Merritt & Tremblay (1994) and Merritt (1996). The starting point is an estimate of the three-dimensional density obtained by replacing each particle at position \mathbf{r}_i by a kernel of width h_i , and summing the kernel densities:

$$\hat{\rho}(\mathbf{r}) = \sum_{i=1}^N \frac{m_i}{h_i^3} K\left(\frac{1}{h_i} |\mathbf{r} - \mathbf{r}_i|\right). \quad (3)$$

Here m_i is the mass associated with the i th particle and K is a normalized kernel function, i.e., a density function with unit volume. We adopted the Gaussian kernel,

$$K(y) = \frac{1}{(2\pi)^{3/2}} e^{-y^2/2}. \quad (4)$$

The density estimate of equation (3) has no imposed symmetries. We now suppose that $\rho(\mathbf{r}) = \rho(r)$, i.e., that the underlying density is spherically symmetric about the origin. In order for the density estimate to have this property, we assume that each particle is smeared uniformly around the surface of the sphere whose radius is r_i . The spherically symmetrized density estimate is

$$\hat{\rho}(r) = \sum_{i=1}^N \frac{m_i}{h_i^3} \frac{1}{4\pi} \int d\phi \int d\theta \sin\theta K\left(\frac{d}{h_i}\right), \quad (5a)$$

$$d^2 = |\mathbf{r} - \mathbf{r}_i|^2 \quad (5b)$$

$$= r_i^2 + r^2 - 2rr_i \cos\theta, \quad (5c)$$

where θ is defined (arbitrarily) from the \mathbf{r}_i -axis. This can be expressed in terms of the angle-averaged kernel \tilde{K} ,

$$\begin{aligned} \tilde{K}(r, r_i, h_i) &\equiv \frac{1}{4\pi} \int_{-\pi/2}^{\pi/2} d\phi \\ &\times \int_0^{2\pi} d\theta \sin\theta K\left(h_i^{-1} \sqrt{r_i^2 + r^2 - 2rr_i \cos\theta}\right) \end{aligned} \quad (6a)$$

$$= \frac{1}{2} \int_{-1}^1 d\mu K\left(h_i^{-1} \sqrt{r_i^2 + r^2 - 2rr_i\mu}\right), \quad (6b)$$

as

$$\hat{\rho}(r) = \sum_{i=1}^N \frac{m_i}{h_i^3} \tilde{K}(r, r_i, h_i). \quad (7)$$

Substituting for the Gaussian kernel, we find

$$\tilde{K}(r, r_i, h_i) = \frac{1}{(2\pi)^{3/2}} \left(\frac{rr_i}{h_i^2}\right)^{-1} \exp\left(-\frac{r_i^2 + r^2}{2h_i^2}\right) \sinh\left(\frac{rr_i}{h_i^2}\right). \quad (8)$$

A computationally preferable form is

$$\tilde{K} = \frac{1}{2(2\pi)^{3/2}} \left(\frac{rr_i}{h_i^2}\right)^{-1} \left\{ \exp\left[-\frac{(r_i - r)^2}{2h_i^2}\right] - \exp\left[-\frac{(r_i + r)^2}{2h_i^2}\right] \right\}. \quad (9)$$

Equations (7) and (9) define the density estimate. Typically, one sets up a grid in radius and evaluates $\hat{\rho}(r)$ discretely on the grid. However, we stress that the density estimate itself is a continuous function and is defined independently of any grid.

Given a sample of N positions and particle masses drawn randomly from some (unknown) $\rho(r)$, the goal is to construct an estimate $\hat{\rho}(r)$ that is as close as possible, in some sense, to $\rho(r)$. In the scheme just described, one has the freedom to adjust the N kernel widths h_i in order to achieve this. In general, if the h_i are too small, the density estimate will be “noisy,” i.e., $\hat{\rho}(r)$ will exhibit a large *variance* with respect to the true density, while if the h_i are too large, the density estimate will be oversmoothed, i.e., there will be a large *bias*. (Of course the same is true for binned histograms, although in general the bias-variance tradeoff for histograms is less good than for kernel estimates.) If the true $\rho(r)$ were known a priori, one could adjust the h_i so as to minimize (for instance) the mean square deviation between $\rho(r)$ and $\hat{\rho}(r)$. Since $\rho(r)$ is not known a priori for our halos, some algorithm must be adopted for choosing the h_i . We followed the standard practice (e.g., Silverman 1986, p. 101) of varying the h_i as a power of the local density:

$$h_i = h_0 [\hat{\rho}_{\text{pilot}}(r_i)/g]^{-\alpha}, \quad (10)$$

where $\hat{\rho}_{\text{pilot}}(r)$ is a “pilot” estimate of $\rho(r)$, and g is the geometric mean of the pilot densities. Since the pilot estimate is used only for assigning the h_i , it need not be differentiable, and we constructed it using a nearest-neighbor scheme.

The final density estimate $\hat{\rho}(r)$ is then a function of two quantities: h_0 and α . Figure 1 illustrates the dependence of $\hat{\rho}(r)$ on h_0 when the kernel algorithm is applied to a random sample of 10^6 equal-mass particles generated from an Einasto density profile with $n = 5$, corresponding to typical values observed in Merritt et al. (2005). Each of the density profile estimates of Figure 1 used $\alpha = 0.3$. As expected, for small h_0 the estimate of $\rho(r)$ is noisy but faithful in an average way to the true profile, while for large h_0 $\rho(r)$ is a smooth function but is biased at small radii due to the averaging effect of the kernel. For $\alpha = 0.3$ the “optimum” h_0 for this sample is $\sim 0.05r_e$, where r_e is the half-mass radius coming from the Einasto model (see § 4.2).

In what follows we compare the nonparametric estimates $\hat{\rho}(r)$ derived from the N -body models with various parametric fitting functions in order to find the best-fitting parameters of the latter by minimizing the rms residuals between the two profiles. For this purpose, any of the density estimates in Figure 1 would yield similar results, excepting perhaps the density estimate in the top panel, which is clearly biased at small radii. In addition, we also wish to characterize the rms value of the deviation between the “true” profile and the best-fitting parametric models. Here it is useful for the kernel widths to be chosen such that the residuals are dominated by the systematic differences between the parametric and nonparametric profiles, and not by noise in $\hat{\rho}(r)$ resulting from overly small kernels. We verified that this condition was easily satisfied for all of the N -body models analyzed here: there was always found to be a wide range of (h_0, α) values such that the residuals between $\hat{\rho}(r)$ and the parametric function were nearly

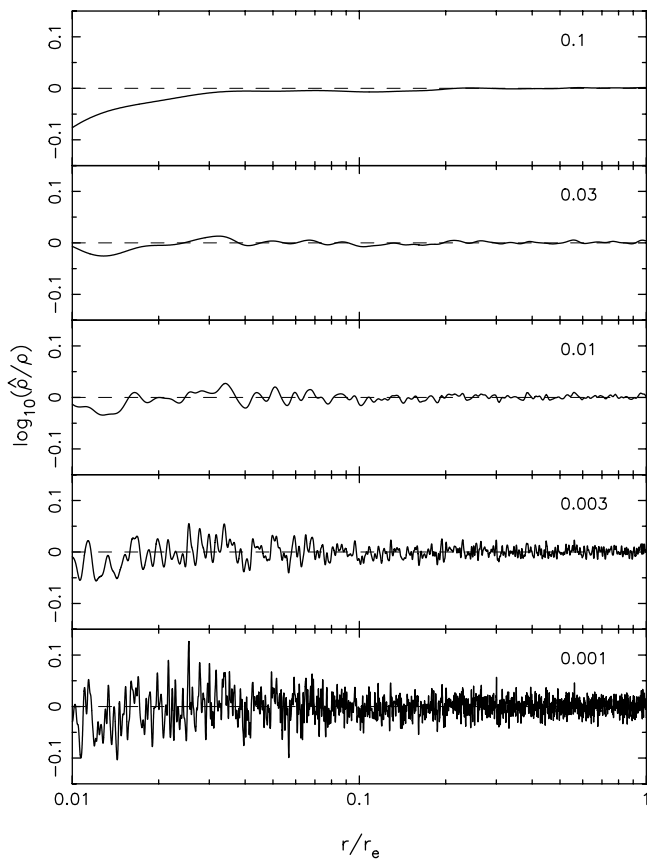


FIG. 1.—Nonparametric bias-variance tradeoff in the estimation of $\rho(r)$ using a single sample of 10^6 radii generated from a halo having an Einasto $r^{1/n}$ density profile with $n = 5$ (see § 4.2). From top to bottom, $h_0 = (0.1, 0.03, 0.01, 0.003, 0.001)r_e$; all estimates use $\alpha = 0.3$ (see eqs. [7], [9], and [10]).

constant. This is a consequence of the large particle numbers ($>10^6$) in the N -body models, which imply a low variance even for small h_0 .

As discussed above, quantities like the derivative of the density can also be computed directly from $\hat{\rho}(r)$. Figure 2 shows nonparametric estimates of the slope, $d \log \hat{\rho} / d \log r$, for the same 10^6 particle data set as in Figure 1. We computed derivatives simply by numerically differentiating $\hat{\rho}(r)$; alternatively, we could have differentiated equation (9). Figure 2 shows that as h_0 is increased, the variance in the estimated slope drops, and for $h_0 \approx 0.2r_e$ the estimate is very close to the true function. We note that the optimal choice of h_0 when estimating derivatives is larger than when estimating $\rho(r)$ ($\sim 0.2r_e$ vs. $\sim 0.05r_e$); this is a well-known consequence of the increase in “noise” associated with differentiation. Figure 2 also illustrates the important point that there is no need to impose an additional level of smoothing when computing the density derivatives (as was done, e.g., in Reed et al. 2005); it is sufficient to increase h_0 .

3.1. Application to the N -Body Halos

Figure 3 shows, using $\alpha = 0.3$ and $h_0 = 0.05r_e$ (left) and $\alpha = 0.4$ and $h_0 = 0.05r_e$ (right),² the nonparametric estimates of $\rho(r)$ (left) and $\gamma(r) \equiv d \log \rho / d \log r$ (right) for the 10 N -body halos. Figure 4 shows the same quantities for the two data sets gener-

² We have intentionally used a small value of h_0 to avoid any possibility of biasing the slope estimates.

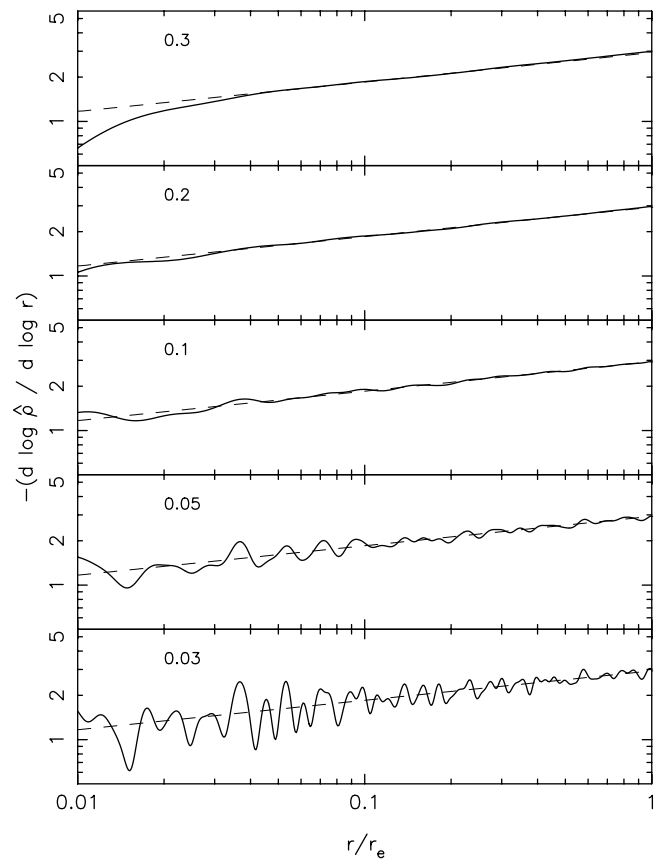


FIG. 2.—Five estimates of the logarithmic slope of an Einasto $r^{1/n}$ halo, derived via differentiation of $\hat{\rho}(r)$. The same sample of 10^6 radii was used as in Fig. 1. From top to bottom, $h_0 = (0.3, 0.2, 0.1, 0.05, 0.03)r_e$; all estimates use $\alpha = 0.4$ (see eq. [10]). Dashed lines show the true slope.

ated from cold collapses. We stress that these plots—especially the derivative plots—could not have been made from tables of binned particle numbers. For most profiles the slope is a rather continuous function of radius and does not appear to reach any obvious, asymptotic, central value by $\sim 0.01r_{\text{vir}}$. Instead, $\hat{\gamma}(r)$ varies approximately as a power of r ; i.e., $\log \hat{\gamma}$ versus $\log r$ is approximately a straight line. Accordingly, we have fitted straight lines, via a least-squares minimization, to the logarithmic profile slopes in the right panels of Figures 3 and 4. The regression coefficients, i.e., slopes, are inset in each panel. (These slope estimates should be seen as indicative only; they are superseded by the model fits discussed below.) In passing we note that such a power-law dependence of γ on r is characteristic of the Einasto model, with the logarithmic slope equal to the exponent $1/n$. Noise and probable (small) deviations from a perfect Einasto $r^{1/n}$ model are expected to produce slightly different exponents when we fit the density profiles in the following section with Einasto’s $r^{1/n}$ model and a number of other empirical functions.

The slope at the innermost resolved radius is always close to -1 , which is also the slope at $r = 0$ in the NFW model. However, there is no indication in Figure 3 that $\hat{\gamma}(r)$ is flattening at small radii; i.e., it is natural to conclude that N -body simulations of higher resolution would exhibit smaller inner slopes. On average, the slope at r_{vir} is around -3 , but there are large fluctuations, and some halos reach a value of -4 , as previously noted in Diemand et al. (2004b). The reason for these fluctuations may be because the outer parts are dynamically very young (i.e., measured in local dynamical times), and they have only partially completed their

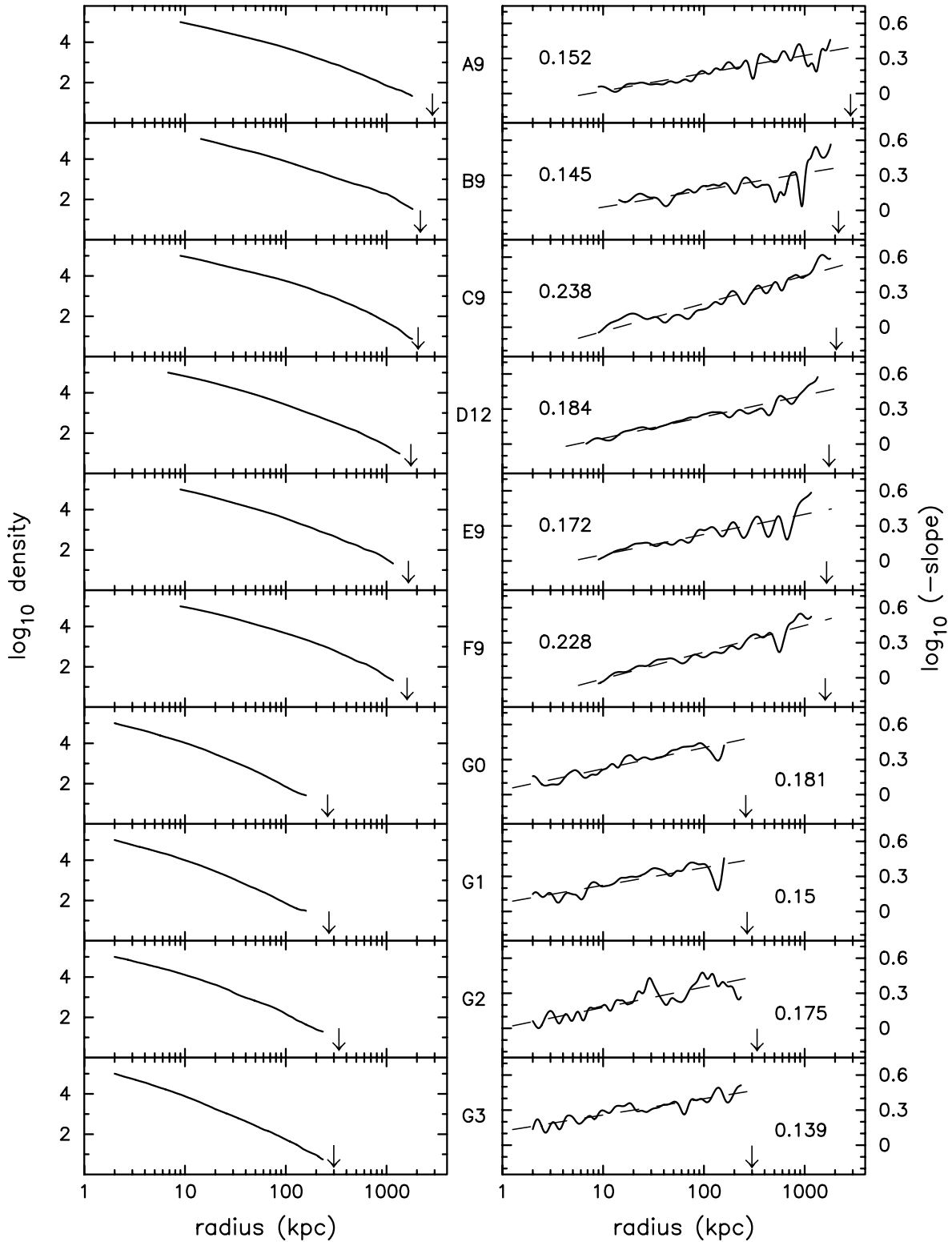


FIG. 3.—Nonparametric estimates of the density $\rho(r)$ (left) and the slope $d \log \rho / d \log r$ (right) for the 10 N -body halos of Table 1. The virial radius r_{vir} is marked with an arrow. Dashed lines in the right panels are linear fits of $\log(-d \log \rho / d \log r)$ to $\log r$; regression coefficients are also given.

evolution to an equilibrium configuration. We are not able to say with any confidence what the slopes do beyond r_{vir} .

4. EMPIRICAL MODELS

In this section we present four parametric density models, each having three independent parameters: two “scaling” parameters

and one “shape” parameter. We measured the quality of each parametric model’s fit to the nonparametric $\hat{\rho}(r)$ values using a standard metric, the integrated square deviation,

$$\int d(\log r) [\log \hat{\rho}(r) - \log \rho_{\text{param}}(r)]^2, \quad (11)$$

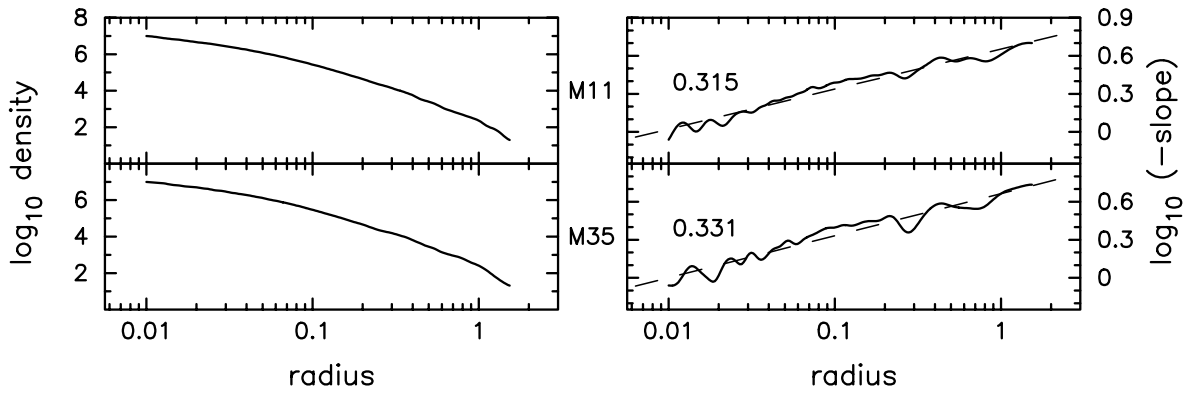


FIG. 4.—Nonparametric estimates of $\rho(r)$ (left) and $d \log \rho / d \log r$ (right) for the two “collapse” models. Dashed lines in the right panels are linear fits of $\log(-d \log \rho / d \log r)$ to $\log r$.

where ρ_{param} is understood to depend on the various fitting parameters, as well as on r . Equation (11) is identical in form to the Cramér–von Mises statistic (e.g., Cox & Hinkley 1974, eq. [6]), an alternative to the Kolmogorov–Smirnov statistic for comparing two (cumulative) distribution functions.

We chose to evaluate this integral by discrete summation on a grid spaced uniformly in $\log r$; our measure of goodness of fit (which was also the quantity that was minimized in determining the best-fit parameters) was

$$\Delta^2 \equiv \frac{\sum_{j=1}^m \delta_j^2}{m-3}, \quad (12a)$$

$$\delta_j = \log \left[\frac{\hat{\rho}(r_j)}{\rho_{\text{param}}(r_j)} \right], \quad (12b)$$

with $m = 300$. With such a large value of m the results obtained by minimizing equations (12a) and (11) are indistinguishable. We note that the quantity Δ^2 in equation (12a) is reminiscent of the standard χ^2 , but the resemblance is superficial. For instance, Δ^2 as defined here is independent of m in the large- m limit (and our choice of $m = 300$ puts us effectively in this limit). Furthermore, there is no binning involved in the computation of Δ^2 ; the grid is simply a numerical device used in the computation of equation (11).

4.1. Double-Power-Law Models

Hernquist (1990, his eq. [43]) presented a five-parameter generalization of Jaffe’s (1983) double-power-law model. Sometimes referred to as the (α, β, γ) model, it can be written as

$$\rho(r) = \rho_s 2^{(\beta-\gamma)/\alpha} \left(\frac{r}{r_s} \right)^{-\gamma} \left[1 + \left(\frac{r}{r_s} \right)^\alpha \right]^{(\gamma-\beta)/\alpha}, \quad (13)$$

where ρ_s is the density at the scale radius r_s , which marks the center of the transition region between the inner and outer power laws having slopes of $-\gamma$ and $-\beta$, respectively. The parameter α controls the sharpness of the transition (see Zhao 1996; Kravtsov et al. 1998; and eqs. [37] and [40b] in Dehnen & McLaughlin 2005). Setting $(\alpha, \beta, \gamma) = (1, 3, 1)$ yields the NFW model, while $(1.5, 3, 1.5)$ gives the model in Moore et al. (1999). Other combinations have been used: for example, $(1, 3, 1.5)$ was applied in Jing & Suto (2000), and $(1, 2.5, 1)$ was used by Rasia et al. (2004).

In fitting dark matter halos, Klypin et al. (2001, their Fig. 8) have noted a certain degree of degeneracy when all five parameters are allowed to vary. Graham et al. (2003, their Figs. 3 and 4) have also observed the parameters of this empirical model to be highly unstable when applied to (light) profiles having a continuously changing logarithmic slope. Under such circumstances, the parameters can be a strong function of the fitted radial extent rather than reflecting the intrinsic physical properties of the profile under study. This was found to be the case for the dark matter halos under study here. We have therefore chosen to constrain two of the model parameters, holding α fixed at 1 and β fixed at 3.

In recent years, as the resolution in N -body simulations has improved, Moore and collaborators have found that the innermost (resolved) logarithmic slope of dark matter halos has a range of values that are typically shallower than -1.5 , recently obtaining a mean value (plus or minus a standard deviation) equal to -1.26 ± 0.17 at 1% of the virial radius (Diemand et al. 2004b). At the same time, Navarro et al. (2004) report that the NFW model underestimates the density over the inner regions of most of their halos, which have innermost resolved slopes ranging from -1.6 to -0.95 (their Fig. 3). A model with an outer slope of -3 and an inner slope of $-\gamma$ might therefore be more appropriate. Such a model has been used before and can be written as

$$\rho(r) = \frac{2^{3-\gamma} \rho_s}{(r/r_s)^\gamma (1 + r/r_s)^{3-\gamma}}. \quad (14)$$

The total mass of this model is infinite, however.

We have applied the above $(1, 3, \gamma)$ model to our dark matter density profiles, the results of which are shown in Figure 5 for the N -body halos, and in the top panel of Figure 6 for the cold-collapse models. The rms scatter Δ is inset in each figure and additionally reported in Table 1.

4.1.1. Two-Parameter Models

Recognizing that galaxies appear to have flat inner density profiles (e.g., Flores & Primack 1994; Moore 1994), Burkert (1995) cleverly introduced a density model having an inner slope of zero and an outer profile that decayed as r^{-3} . His model is given by the expression

$$\rho(r) = \frac{\rho_0 r_s^3}{(r + r_s)(r^2 + r_s^2)}, \quad (15)$$

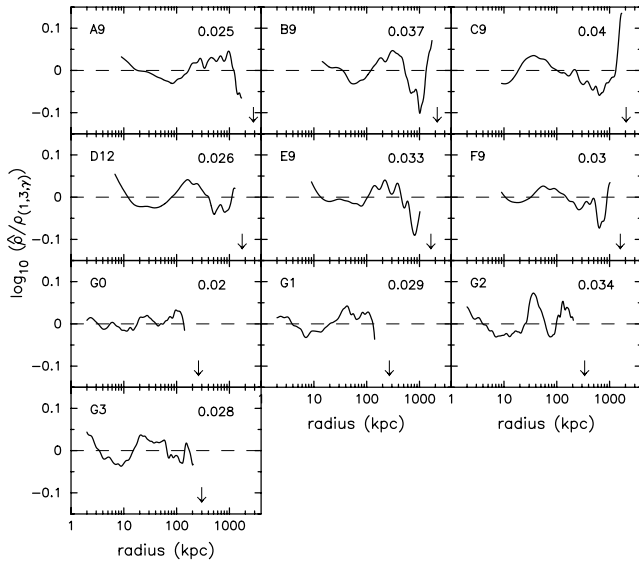


FIG. 5.—Residual profiles from application of the three-parameter $(1, 3, \gamma)$ model (eq. [14]) to our 10 N -body density profiles. The virial radius is marked with an arrow, and the rms residual (eq. [12a]) is inset with the residual profiles.

where ρ_0 is the central density and r_s is a scale radius. Application of this model in Figure 7 reveals that, with only two free parameters, it does not provide as good a fit to the simulated dark matter halos as the $(1, 3, \gamma)$ model presented above. The hump-shaped residual profiles in Figure 7 signify the model’s inability to match the curvature of our density profiles. (It is important to point out that Burkert’s model was introduced to fit the observed rotation curves in low surface brightness galaxies after the contribution from the baryonic component had been subtracted out, a task that it performs well.) This and other two-parameter models are shown in Table 2.

As noted previously, the NFW $(\alpha, \beta, \gamma) = (1, 3, 1)$ model also has only two parameters: ρ_s and r_s . Because this model is still often used, we apply it to our halos in Figure 8. Comparison with Figure 5 reveals that the NFW model never performs as well as the $(1, 3, \gamma)$ model; the residuals are $\sim 50\%$ larger and sometimes twice as large. Importantly, the large-scale curvature observed in many of the NFW residual profiles (Fig. 8) reveals that this model does not describe the majority of the halos, and that the $(1, 3, \gamma)$ model should be preferred over the NFW model.

An alternative two-parameter expression has recently been studied by Dehnen & McLaughlin (2005, their eq. [20b]; see also Austin et al. 2005). It is a special case of a more general family of models, which we test next, when the velocity ellipsoid at the halo center is isotropic and ρ/σ_r^3 is a (special) power law in radius, varying as $r^{-35/18}$. This two-parameter density model is an $(\alpha, \beta, \gamma) = (4/9, 31/9, 7/9)$ model given by

$$\rho(r) = \frac{2^6 \rho_s}{(r/r_s)^{7/9} [1 + (r/r_s)^{4/9}]^6}, \quad (16)$$

and is applied in Figure 9. It clearly provides a much better match to the dark matter halo density profiles in comparison with the previous two-parameter model over the fitted radial range, but the rms scatter reveals that it does not perform as well as the $(1, 3, \gamma)$ model, nor can it describe the “spherical collapse” halos (Fig. 6). Therefore, in § 4.1.2 we test the more general three-parameter model given in Dehnen & McLaughlin (2005).

4.1.2. Dehnen-McLaughlin Anisotropic Three-Parameter Model

Dehnen & McLaughlin (2005, their eq. [46b]) present a theoretically motivated, three-parameter model such that

$$[\alpha, \beta, \gamma] = [2(2 - \beta_0)/9, (31 - 2\beta_0)/9, (7 + 10\beta_0)/9],$$

and the term β_0 reflects the central ($r = 0$) anisotropy: a measure of the tangential to radial velocity dispersion.³ Setting $\gamma' = (7 + 10\beta_0)/9$, we have $[\alpha, \beta, \gamma] = [(3 - \gamma')/5, (18 - \gamma')/5, \gamma']$, and their density model can be written as

$$\rho(r) = \frac{2^6 \rho_s}{(r/r_s)^{\gamma'} [1 + (r/r_s)^{(3-\gamma')/5}]^6}, \quad (17)$$

As shown in Figure 10, for three of the six cluster-sized halos this model has the greatest residual scatter of the four different three-parameter models tested here. For another two of the six cluster-sized halos it has the second greatest residual scatter. This model is also unable to match the curvature in the halos of the cold-collapse models (Fig. 10). However, it does provide very good fits to the galaxy-sized halos, and actually has the smallest residual scatter for three of these halos (Table 3).

The shallowest, inner, negative logarithmic slope of this model occurs when $\beta_0 = 0$, giving a value of $7/9 \approx 0.78$. For nonzero values of β_0 this slope steepens roughly linearly with β_0 .

4.2. Sérsic/Einasto Model

Sérsic (1963, 1968) generalized de Vaucouleurs’s (1948) $R^{1/4}$ luminosity profile model by replacing the exponent $1/4$ with $1/n$, such that n was a free parameter that measured the “shape” of a galaxy’s luminosity profile. Using the observers’ notion of “concentration” (see the review in Graham et al. 2001), the quantity n is monotonically related to how centrally concentrated a galaxy’s light profile is. With R denoting the projected radius, Sérsic’s $R^{1/n}$ model is often written as

$$I(R) = I_e \exp\left\{-b_n \left[\left(R/R_e\right)^{1/n} - 1\right]\right\}, \quad (18)$$

where I_e is the (projected) intensity at the (projected) effective radius R_e . The term b_n is not a parameter but a function of n and defined in such a way that R_e encloses half of the (projected) total galaxy light (Caon et al. 1993; see also Ciotti 1991, his eq. [1]). A good approximation when $n \gtrsim 0.5$ is given in Prugniel & Simien (1997) as

$$b_n \approx 2n - 1/3 + 0.009876/n. \quad (19)$$

Assorted expressions related to the $R^{1/n}$ model can be found in Graham & Driver’s (2005) review article.

Despite the success of this model in describing the luminosity profiles of elliptical galaxies (e.g., Davies et al. 1988; Caon et al. 1993; D’Onofrio et al. 1994; Young & Currie 1995; Graham et al. 1996; Graham & Guzmán 2003; and references therein), it is nonetheless an empirical fitting function with no commonly recognized physical basis (but see Binney et al. 1982; Merritt et al. 1989; Ciotti 1991; Márquez et al. 2001). We are therefore free to explore the suitability of this function for describing the *mass*

³ The quantities β and β_0 are not as related as their notation suggests. The former is the outermost, negative logarithmic slope of the density profile, while the latter is the velocity anisotropy parameter at $r = 0$.

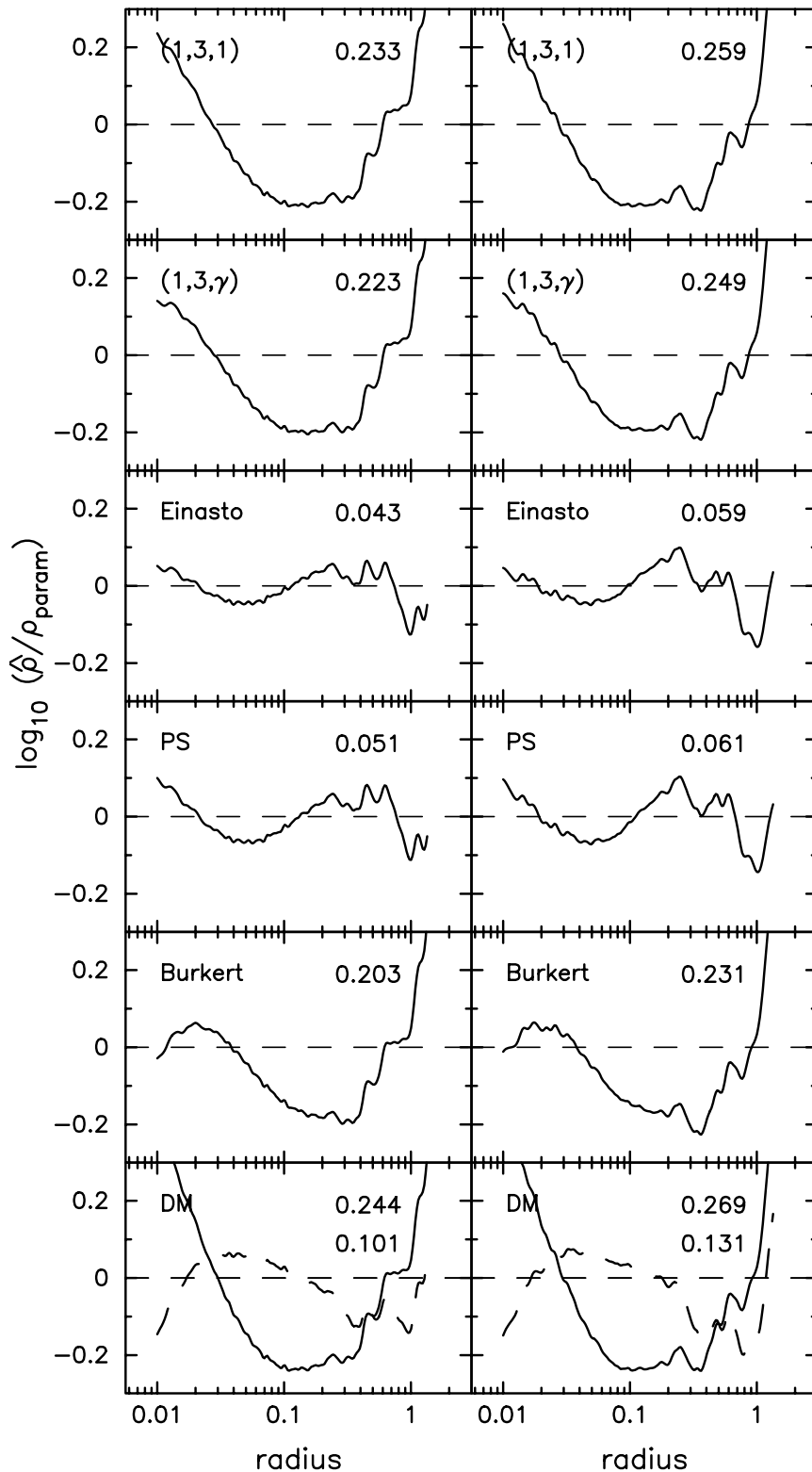


FIG. 6.—Residual profiles from the application of seven different parametric models (see § 4) to our cold-collapse density halos, M11 and M35. In the bottom panel, the solid curve corresponds to the two-parameter model from Dehnen & McLaughlin (2005), and the dashed curve corresponds to their three-parameter model. The rms residual (eq. [12a]) is inset in each figure.

density profiles, $\rho(r)$, of dark matter halos. Indeed, Einasto (1965, eq. [4]; 1968, eq. [1.7]; 1969, eq. [3.1]) independently developed the functional form of Sérsic's equation and used it to describe density profiles. More recent application of this profile to the modeling of density profiles can be found in Einasto & Haud (1989,

their eq. [14]) and Tenjes et al. (1994, their eq. [A1]). Most recently, the same model has been applied by Navarro et al. (2004) and Merritt et al. (2005) to characterize dark matter halos, and Aceves et al. (2006) used it to describe merger remnants in simulated disk galaxy collisions.

TABLE 1
EMPIRICAL THREE-PARAMETER MODELS

HALO ID (1)	(1, 3, γ)				EINASTO $r^{1/n}$				PRUGNIEL-SIMIEN			
	r_s (kpc) (2)	$\log \rho_s$ ($M_\odot \text{ pc}^{-3}$) (3)	γ (4)	Δ (dex) (5)	r_e (kpc) (6)	$\log \rho_e$ ($M_\odot \text{ pc}^{-3}$) (7)	n_{Ein} (8)	Δ (dex) (9)	R_e (kpc) (10)	$\log \rho'$ ($M_\odot \text{ pc}^{-3}$) (11)	n_{PS} (12)	Δ (dex) (13)
Cluster-sized Halos												
A09.....	626.9	-3.87	1.174	0.025	5962	-6.29	6.007	(0.015)	2329	-2.73	3.015	0.021
B09.....	1164	-4.75	1.304	(0.037)	17380	-7.66	7.394	0.041	4730	-3.34	3.473	0.038
C09.....	241.8	-3.27	0.896	0.040	1247	-4.95	3.870	0.030	738.9	-2.55	2.192	(0.016)
D12.....	356.1	-3.82	1.251	0.026	2663	-6.02	5.939	0.020	1232	-2.52	3.147	(0.019)
E09.....	382.5	-3.96	1.265	0.033	2611	-6.06	5.801	0.032	1231	-2.62	3.096	(0.030)
F09.....	233.9	-3.51	1.012	0.030	1235	-5.26	4.280	0.025	697.3	-2.63	2.400	(0.017)
Galaxy-sized Halos												
G00.....	27.96	-3.16	1.163	(0.020)	189.0	-5.22	5.284	0.023	114.4	-42.02	3.135	0.028
G01.....	35.34	-3.36	1.275	0.029	252.6	-5.51	5.873	(0.028)	146.0	-2.01	3.425	0.032
G02.....	53.82	-3.59	1.229	0.034	391.4	-5.74	5.725	(0.031)	214.9	-2.34	3.243	0.036
G03.....	54.11	-3.70	1.593	0.028	405.6	-5.98	7.791	(0.023)	229.1	-1.47	4.551	0.024
Spherical-Collapse Halos												
M11.....	0.0175	2.66	0.006	0.223	0.244	0.27	3.426	(0.043)	0.187	2.57	2.445	0.051
M35.....	0.0180	1.62	0.030	0.249	0.240	-0.70	3.214	(0.059)	0.185	1.47	2.301	0.061

NOTES.— Col. (1): Object identification. Cols. (2)–(5): (1, 3, γ) model (eqs. [13] and [14]) scale radius r_s , scale density ρ_s , inner profile slope γ , and rms scatter of the fit. Cols. (6)–(9): Einasto $r^{1/n}$ model half-mass radius r_e , associated density ρ_e , profile shape n_{Ein} , and rms scatter of the fit. Cols. (10)–(13): Prugniel-Simien model scale radius R_e , scale density ρ' (the spatial density ρ_e at $r = R_e$ is such that $\rho_e = \rho' e^{-b}$), profile shape n_{PS} , and rms scatter of the fit. Note that the radius and density units do not apply to M11 and M35. For each halo, of the three models shown here, the model having the lowest residual scatter is placed in parentheses.

To avoid potential confusion with Sérsic’s $R^{1/n}$ model, we define the following expression as Einasto’s $r^{1/n}$ model:

$$\rho(r) = \rho_e \exp\left\{-d_n \left[\left(r/r_e\right)^{1/n} - 1\right]\right\}, \quad (20)$$

where r is the *spatial* (i.e., not projected) radius. The term d_n , defined below, is a function of n such that ρ_e is the density at the radius r_e that defines a volume containing half of the total mass. The central density is finite and given by $\rho(r = 0) = \rho_e e^{d_n}$.

The integral of equation (20) over some volume gives the enclosed mass, which is also finite and equal to

$$M(r) = 4\pi \int_0^r \rho(\bar{r}) \bar{r}^2 d\bar{r}. \quad (21)$$

This can be solved by using the substitution $\bar{x} \equiv d_n(\bar{r}/r_e)^{1/n}$ to give

$$M(r) = 4\pi n r_e^3 \rho_e e^{d_n} d_n^{-3n} \gamma(3n, x), \quad (22)$$

where $\gamma(3n, x)$ is the incomplete gamma function defined by

$$\gamma(3n, x) = \int_0^x e^{-t} t^{3n-1} dt. \quad (23)$$

Replacing $\gamma(3n, x)$ with $\Gamma(3n)$ in equation (22) gives the total mass M_{tot} .

The value of d_n , which we first saw in equation (20), is obtained by solving $\Gamma(3n) = 2\gamma(3n, d_n)$, where Γ is the (complete) gamma function. The value of d_n can be well approximated (G. A. Mamon 2005, private communication) by the expression

$$d_n \approx 3n - 1/3 + 0.0079/n, \text{ for } n \gtrsim 0.5 \quad (24)$$

(see Fig. 11).

In Paper II we recast Einasto’s $r^{1/n}$ model using the radius r_{-2} , where the logarithmic slope of the density profile equals -2 .

Einasto’s $r^{1/n}$ model (see Einasto & Haud 1989) was used in Navarro et al. (2004, their eq. [5]) to fit their simulated dark matter

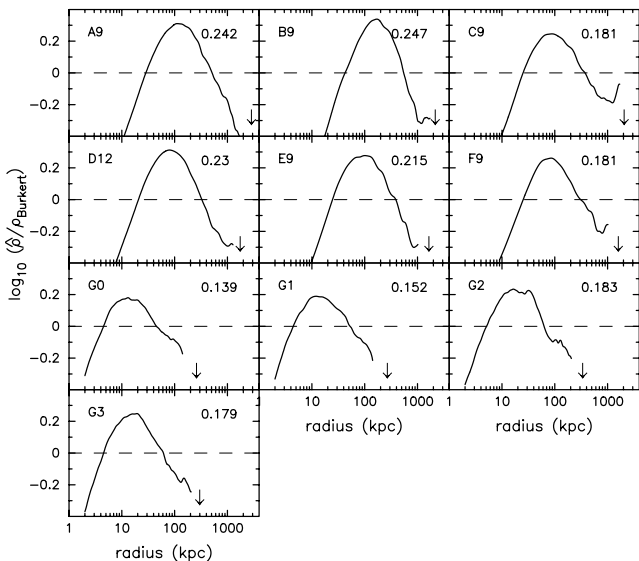


FIG. 7.—Residual profiles from application of Burkert’s two-parameter model (eq. [15]) to our dark matter density profiles.

TABLE 2
TWO-PARAMETER MODELS

HALO ID (1)	BURKERT			NFW			ISOTROPIC DEHNEN-McLAUGHLIN (Eq. [16])		
	r_s (kpc) (2)	$\log \rho_0$ ($M_\odot \text{ pc}^{-3}$) (3)	Δ (dex) (4)	r_s (kpc) (5)	$\log \rho_s$ ($M_\odot \text{ pc}^{-3}$) (6)	Δ (dex) (7)	r_s (kpc) (8)	$\log \rho_s$ ($M_\odot \text{ pc}^{-3}$) (9)	Δ (dex) (10)
Cluster-sized Halos									
A09.....	114.0	-1.65	0.242	419.8	-3.50	0.042	933.7	-2.43	(0.018)
B09.....	145.2	-2.23	0.247	527.2	-4.03	0.068	1180.0	-2.97	(0.042)
C09.....	96.16	-1.74	0.181	284.4	-3.42	(0.042)	554.3	-2.27	0.091
D12.....	68.39	-1.62	0.230	213.3	-3.34	0.051	409.1	-2.17	(0.026)
E09.....	77.09	-1.80	0.215	227.0	-3.46	0.053	428.2	-2.28	(0.037)
F09.....	80.17	-1.85	0.181	229.0	-3.49	(0.030)	438.2	-2.32	0.066
Galaxy-sized Halos									
G00.....	10.12	-1.56	0.139	22.23	-2.94	(0.024)	34.43	-1.59	0.037
G01.....	10.28	-1.54	0.152	23.12	-2.95	0.038	36.53	-1.61	(0.031)
G02.....	14.06	-1.66	0.183	36.39	-3.22	0.044	63.06	-1.96	(0.035)
G03.....	09.35	-1.32	0.179	19.54	-2.68	0.066	26.98	-1.23	(0.025)
Spherical-Collapse Halos									
M11.....	0.0261	3.01	(0.203)	0.0309	2.23	0.233	0.0234	4.31	0.244
M35.....	0.0265	1.98	(0.231)	0.0314	1.20	0.259	0.0236	3.29	0.269

NOTES.—Col. (1): Object identification. Cols. (2)–(4): Burkert (1995) model scale radius r_s , central density ρ_0 , and rms scatter of the fit (using $m - 2$ in the denominator of eq. [12a]). Cols. (5)–(7): NFW (1, 3, 1) model scale radius r_s , scale density ρ_0 , and rms scatter of the fit (using $m - 2$). Cols. (8)–(10): Dehnen & McLaughlin (2005, their eq. [20b]) model scale radius r_s , associated density ρ_s , and rms scatter (using $m - 2$). This model has inner and outer negative logarithmic slopes of $7/9 \approx 0.78$ and $31/9 \approx 3.44$, respectively. Note that the above radius and density units do not apply to M11 and M35. For each halo, the two-parameter model with the lowest residual scatter is placed in parentheses.

halos. They obtained $n \approx 1/(0.172 \pm 0.032) \approx 6 \pm 1.1$. Subsequently, Merritt et al. (2005) showed that Einasto's $r^{1/n}$ model performed as well as the (1, 3, γ) model and gave better fits for the dwarf galaxy- and galaxy-sized halos, obtaining $n \approx 5.6 \pm 0.7$. For a sample of galaxy-sized halos, Prada et al. (2006) obtained similar values of 6–7.5.

Figure 12 shows the application of equation (20) to the N -body halos of § 3. A comparison with the (1, 3, γ) model fits in Figure 5 reveals that Einasto's model provides a better descrip-

tion for five of the six cluster-sized halos, three of the four galaxy-sized halos, and both of the spherical-collapse halos.

Navarro et al. (2004) wrote “adjusting the parameter [n] allows the profile to be tailored to each individual halo, resulting in improved fits.”⁴ Such a breaking of structural homology (see

⁴ The value of n , equal to $1/\alpha$ in Navarro et al.'s (2004) notation, ranged from 4.6 to 8.2 (Navarro et al. 2004, their Table 3).

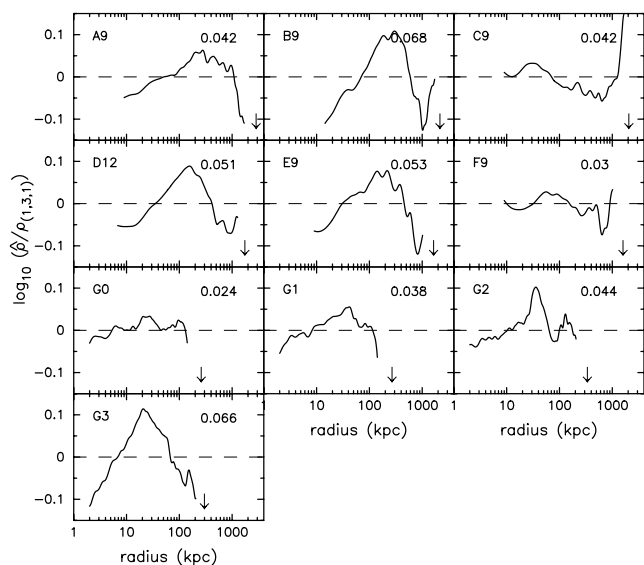


FIG. 8.— Residual profiles from application of the two-parameter NFW (1, 3, 1) model to our dark matter density profiles.

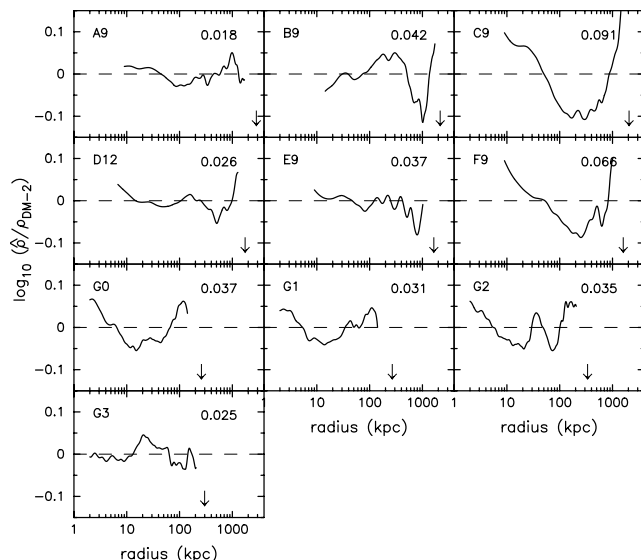


FIG. 9.— Residual profiles from application of the two-parameter (4/9, 31/9, 7/9) model (eq. [16]) from Dehnen & McLaughlin (2005, their eq. [20b]) to our dark matter density profiles.

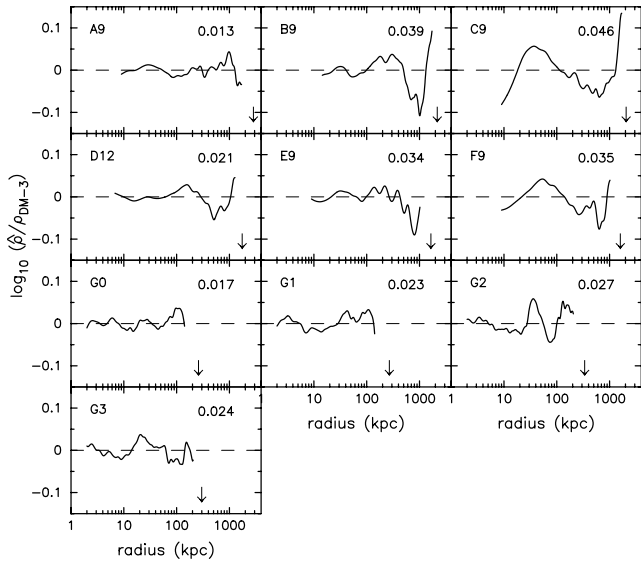


FIG. 10.—Residual profiles from application of the three-parameter $(3 - \gamma')/5, (18 - \gamma')/5, \gamma'$ model (eq. [17]) from Dehnen & McLaughlin (2005, their eq. [46b]) to our dark matter density profiles.

Graham & Colless [1997] for an analogy with projected luminosity profiles) replaces the notion that a universal density profile may exist.

A number of useful expressions pertaining to Einasto’s model, when used as a density profile (eq. [20]), are given in Cardone et al. (2005) and Mamon & Lokas (2005). In particular, Cardone et al. provide the gravitational potential, as well as approximations to the surface density and space velocity dispersion of the Einasto $r^{1/n}$ model, while Mamon & Lokas give approximations

TABLE 3
THEORETICALLY MOTIVATED ANISOTROPIC DEHNEN-McLAUGHLIN
THREE-PARAMETER MODEL

Halo ID (1)	r_s (kpc) (2)	$\log \rho_s$ ($M_\odot \text{ pc}^{-3}$) (3)	γ' (4)	Δ (dex) (5)
Cluster-sized Halos				
A09.....	722.7	-2.21	0.694	(0.013)
B09.....	1722	-3.30	0.880	0.040
C09.....	207.0	-1.34	0.241	0.047
D12.....	322.8	-1.95	0.683	0.022
E09.....	330.4	-2.04	0.669	0.034
F09.....	193.6	-1.56	0.350	0.036
Galaxy-sized Halos				
G00.....	20.89	-1.11	0.422	(0.017)
G01.....	25.88	-1.28	0.568	(0.023)
G02.....	43.05	-1.60	0.581	(0.027)
G03.....	30.20	-1.34	0.849	0.024
Spherical Collapse Halos				
M11.....	0.025	4.23	0.00	0.179
M35.....	0.025	3.21	0.00	0.206

NOTES.—Col. (1): Object identification. Cols. (2)–(5): Dehnen-McLaughlin (their eq. [46b]) scale radius r_s , scale density ρ_s , inner profile slope γ' , and rms scatter of the fit. Note that the radius and density units do not apply to M11 and M35. When the rms scatter is lower than the value obtained with the other three-parameter models, it is placed in parentheses.

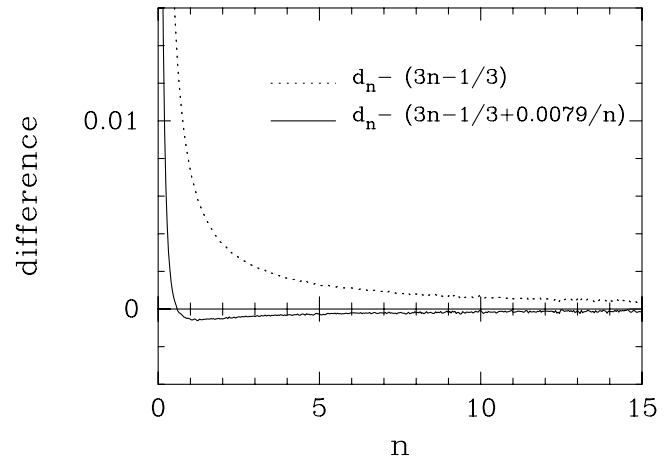


FIG. 11.—Difference between the exact value for d_n from eq. (20) such that $\Gamma(3n) = 2\gamma(3n, d_n)$ and the two approximations inset in the figure.

for the concentration parameter, central density, and $M_{\text{vir}}/M_{\text{tot}}$, the virial-to-total mass ratio. The nature of the inner profile slope of Einasto’s $r^{1/n}$ model and several other useful quantities are presented in Paper II.

4.3. Prugniel-Simien Model: A Deprojected Sérsic $R^{1/n}$ Model

Merritt et al. (2005) tested how well a deprojected Sérsic $R^{1/n}$ model fitted $\rho(r)$ from the Navarro et al. (2004) N -body halos. This was essentially the same as comparing the halo surface densities with Sérsic’s $R^{1/n}$ law. Prugniel & Simien (1997) presented a simple, analytical approximation to the deprojected Sérsic law (their eq. [B6]):

$$\rho(r) = \rho' \left(\frac{r}{R_e} \right)^{-p} \exp \left[-b \left(\frac{r}{R_e} \right)^{1/n} \right], \quad (25)$$

with

$$\rho' = \frac{M}{L} I_e e^b b^{n(1-p)} \frac{\Gamma(2n)}{2R_e \Gamma(n(3-p))}. \quad (26)$$

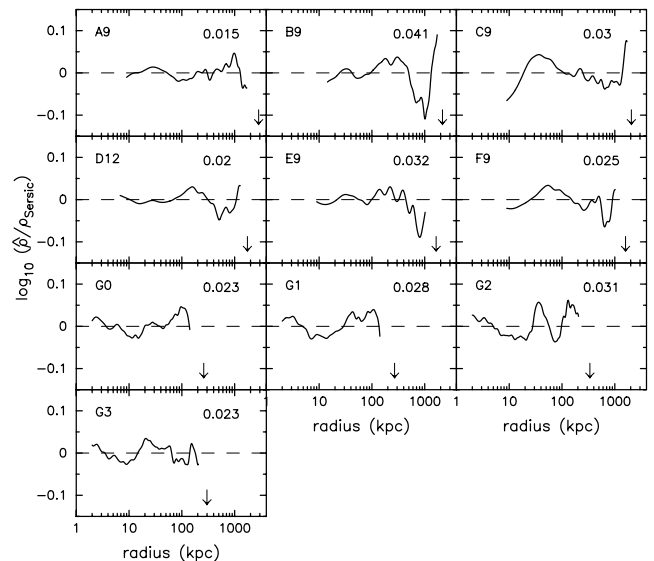


FIG. 12.—Residual profiles from application of Einasto’s $r^{1/n}$ model (eq. [20]) to our dark matter density profiles.

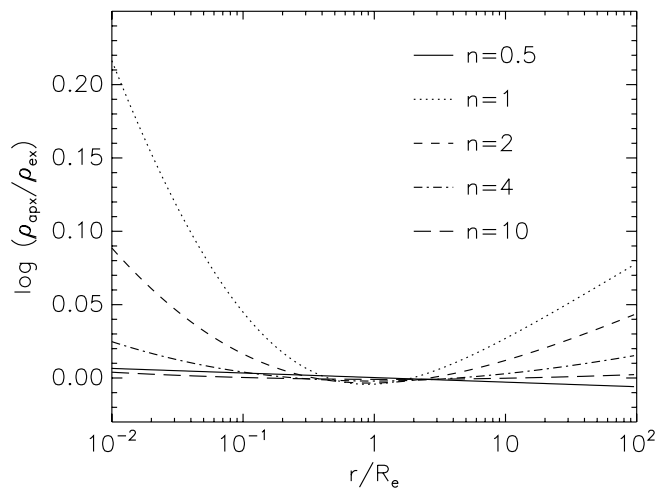


FIG. 13.—Logarithmic difference between the exact deprojection of Sérsic's $R^{1/n}$ model (eq. [18]) and the approximation given by Prugniel & Simien (1997) in eq. (25), using the values of p and b given in eqs. (27) and (19), respectively.

Equation (25) is a generalization of equation (2) in Mellier & Mathez (1987), who considered only approximations to the deprojected $R^{1/4}$ law. Mellier & Mathez's model was itself a modification of equation (33) from Young (1976), which derived from the work of Poveda et al. (1960).

In these expressions, R_e , n , and b are understood to be essentially the same quantities that appear in the Sérsic $R^{1/n}$ law that describes the projected density (eq. [18]). In fact, since equation (25) is not exactly a deprojected Sérsic profile, the correspondence between the parameters will not be perfect. We follow the practice of earlier authors and define b to have the same relation to n as in equation (19). (For clarity, we have dropped the subscript n from b_n .) Although the parameter ρ' is obtained from fitting the density profile, it can be defined in such a way that the total (finite) mass from equation (25) equals that from equation (18), giving equation (26). (We stress that the n in the Prugniel-Simien profile is *not* equivalent to the n in eq. [20], Einasto's model.)

This leaves the parameter p . We define p , like b , uniquely in terms of n :

$$p = 1.0 - 0.6097/n + 0.05463/n^2. \quad (27)$$

Lima Neto et al. (1999) derived this expression by requiring the projection of equation (25) to approximate as closely as possible the Sérsic profile with the same (R_e, n) , for $0.6 \leq n \leq 10$ and $10^{-2} \leq R/R_e \leq 10^3$.⁵ The accuracy of Prugniel & Simien's (1997) approximation, using equation (27) for $p(n)$, is shown in Figure 13.

Terzić & Graham (2005) give simple expressions, in terms of elementary and special functions, for the gravitational potential and force of a galaxy obeying the Prugniel-Simien law and derive the spatial and line-of-sight velocity dispersion profiles.

One could also allow p to be a free parameter, creating a density profile that has any desired inner slope. For instance, setting $p = 0$, the Prugniel-Simien model reduces to the Einasto model. We do not explore that idea further here.

⁵ The value of p given in eq. (27) is preferable to the value $1.0 - 0.6097/n + 0.05563/n^2$ given in Márquez et al. (2000) (G. B. Lima Neto 2005, private communication).

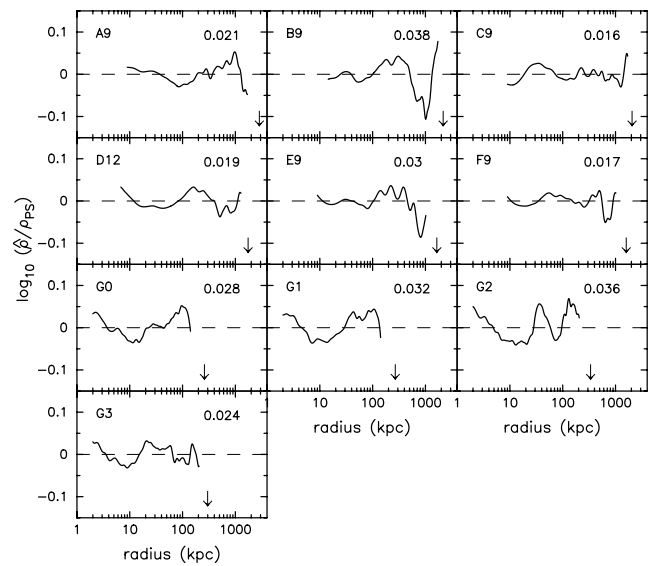


FIG. 14.—Residual profiles from application of the Prugniel-Simien model (eq. [25]) to our dark matter density profiles.

The density at $r = R_e$ is given by $\rho_e = \rho' e^{-b}$, while the projected surface density at $R = R_e$, denoted by I_e , can be solved for using equation (26). Thus, one can immediately construct (a good approximation to) the projected mass distribution, which will have a Sérsic form (eq. [18]) with parameters $(R_e, I_e, \text{ and } n)$. This allows the halo parameters to be directly compared with those of Sérsic fits to luminous galaxies, which we do in Paper III. In Paper II we recast this model using the radius where the logarithmic slope of the density profile equals -2 .

The mass profile (Terzić & Graham 2005, their Appendix A; see also Lima Neto et al. 1999; Márquez et al. 2001) can be written as

$$M(r) = 4\pi\rho'R_e^3 n b^{n(p-3)} \gamma(n(3-p), Z), \quad (28)$$

where $Z \equiv b(r/R_e)^{1/n}$ and $\gamma(a, x)$ is the incomplete gamma function given in equation (23). The total mass is obtained by replacing $\gamma(n(3-p), Z)$ with $\Gamma(n(3-p))$, and the circular velocity is given by $v_{\text{circ}}(r) = [GM(r)/r]^{1/2}$.

In Figure 14 equation (25) has been applied to our dark matter profiles. The average (plus or minus a standard deviation) of the shape parameter for the galaxy-sized and cluster-sized halos is $n = 3.59 \pm 0.65$ and $n = 2.89 \pm 0.49$, respectively. Merritt et al. (2005, their Table 1) found values of 3.40 ± 0.36 and 2.99 ± 0.49 for their sample of galaxies and clusters, respectively, in good agreement with the results obtained here using a different set of N -body simulations.

Figure 14 reveals that CDM halos resemble galaxies (Merritt et al. 2005), since the projection of the Prugniel-Simien model closely matches the Sérsic $R^{1/n}$ model and the latter is a good approximation to the luminosity profiles of stellar spheroids. Subject to vertical and horizontal scaling, CDM halos have mass distributions similar to those of elliptical galaxies with an absolute B -band magnitude around -18 ± 1 mag; these galaxies have $n \sim 3$ (see Graham & Guzmán 2003, their Fig. 9). This result was obscured until recently due to the use of different empirical models by observers and modelers.

Before moving on, we again remark that we have not explored potential refinements to expression (27) for the quantity p , but

TABLE 4
RESIDUAL SCATTER: RMS VALUES OF Δ

Model (1)	Cluster-sized Halos (2)	Galaxy-sized Halos (3)	Spherical-Collapse Halos (4)
Three-Parameter Models			
Einasto.....	(0.028)	(0.026)	(0.052)
Prugniel-Simien.....	(0.025)	0.030	(0.056)
(1, 3, γ).....	0.032	0.028	0.236
Dehnen-McLaughlin (eq. [17]).....	0.034	(0.023)	0.193
Two-Parameter Models			
Dehnen-McLaughlin (eq. [16]).....	0.053	0.032	0.257
NFW.....	0.046	0.046	0.246
Burkert.....	0.218	0.164	0.217

NOTES.— Col. (1): Model. Col. (2): The rms of the six residual scatters, Δ_{rms} (eq. [29]), for the cluster-sized halos. Col. (3): Similar to col. (2) but for the four galaxy-sized halos. Col. (4): Similar to col. (2) but for the two spherical-collapse halos. For each halo type, the two models that perform the best are placed in parentheses.

note that this could result in a better matching of the model to the simulated profiles at small radii. As the resolution of N -body clustering simulations continues to improve, it will make sense to explore such generalizations.

5. MODEL COMPARISON: WHICH DID BEST?

Table 4 summarizes how well each parametric model performed by listing the rms value of Δ (eq. [12a]) for each set of halos, given by

$$\Delta_{\text{rms}} = \sqrt{\frac{1}{N} \sum_{i=1}^N \Delta_i^2}, \quad (29)$$

with $N = 6, 4,$ and 2 for the cluster-sized, galaxy-sized, and spherical-collapse halos, respectively. A detailed description of each model's performance follows.

The bowl- and hump-shaped residual profiles associated with the two-parameter model of Burkert (1995) reveal this model's inability to describe the radial mass distribution in our simulated dark matter halos. The two-parameter model of Dehnen & McLaughlin (2005) performs considerably better, although it too fails to describe the cold-collapse systems and two of the six cluster-sized halos, specifically, C09 and F09. Although this (4/9, 31/9, 7/9) model never provides the best fit, it does equal or outperform the NFW-like (1, 3, γ) model in describing 3 of the 12 halos (A09, D12, and G03).

In general, all of the three-parameter models perform well (0.015 dex $\lesssim \Delta \lesssim$ 0.04 dex) at fitting the N -body (noncollapse) halos. However, neither the (1, 3, γ) model nor the three-parameter Dehnen-McLaughlin model can match the curvature in the density profiles of the cold-collapse systems (M11 and M35). On the other hand, both Einasto's $r^{1/n}$ model and that from Prugniel & Simien give reasonably good fits ($\Delta \sim 0.05$ dex) for these two halos.

The Prugniel-Simien model provided the best overall description of the cluster-sized, N -body halos. The (1, 3, γ) model and the three-parameter Dehnen-McLaughlin model provided the best fit for only one cluster-sized, N -body halo each, and even then the (1, 3, γ) model only just outperformed the Prugniel-Simien model, which gave the best fit for four of the six cluster-sized halos. For two of these halos, the size of the residual about the optimal

Prugniel-Simien fit was roughly half of the value obtained when using the (1, 3, γ) model.

The implication of this result is that Sérsic's $R^{1/n}$ model will describe the projected surface density of the cluster-sized, dark matter halos. Intriguingly, Demarco et al. (2003) and Durret et al. (2005) have observed that the (projected) hot X-ray gas distribution in clusters can indeed be described with Sérsic's $R^{1/n}$ model, although the gas can at times display a rather unrelaxed behavior (Statler & Diehl 2005). Studies of gravitational lensing may therefore benefit from the use of Sérsic's $R^{1/n}$ model for which the lensing equation has been solved (Cardone 2004) and for which numerous other properties have previously been computed (Graham & Driver 2005).

With regard to the galaxy-sized, N -body halos, the situation is somewhat different. Dehnen & McLaughlin's (2005) anisotropic three-parameter model provided the best fit for three of the four profiles, with the Einasto $r^{1/n}$ model providing the best fit for the fourth profile. We also observe that Einasto's model provided better fits than the (1, 3, γ) model for three of the four N -body halos. If this observation holds, namely, that the Prugniel-Simien model describes the density profiles of the cluster-sized halos best, while Dehnen & McLaughlin's three-parameter model provides the best description of the galaxy-sized halos, it would imply that these halos do not have the same structural form. Of course, even if the same model *did* provide the best fit for both types of halo, any variation in the value of the profile shape n , or central isotropy parameter β_0 , would point toward the existence of nonhomology.

While halos of different mass may be systematically better described by different density laws, it is important to emphasize that a *single* density law provides a good fit to *all* of the N -body halos considered here. As Table 4 shows, Einasto's $r^{1/n}$ law has the smallest, or second-smallest, value of Δ_{rms} for galaxy-sized, cluster-sized, and spherical-collapse halos. None of the other parametric models that we considered performs as well "across the board." The next best performer overall is the Prugniel-Simien profile.

6. DISCUSSION

Figure 15 shows our N -body halos, together with real elliptical galaxies and clusters, in the profile shape versus mass plane. The profile shape parameter plotted there is either n from the Sérsic $R^{1/n}$ model fit to the light profile, or the corresponding parameter

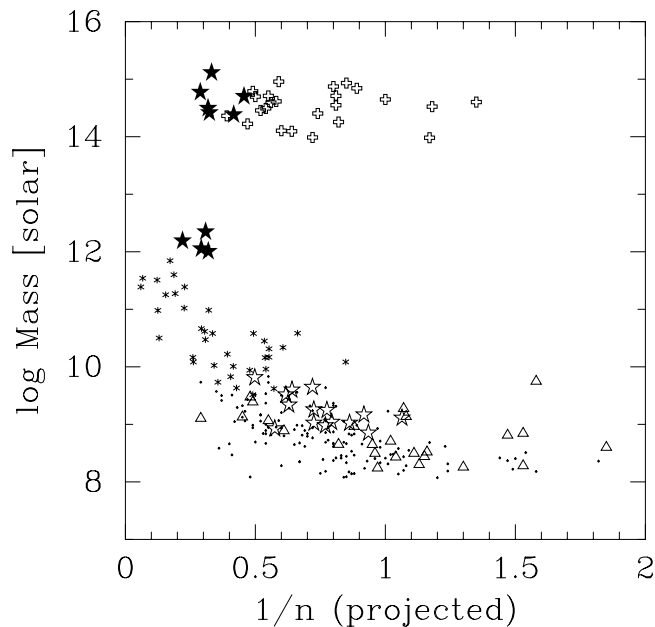


FIG. 15.—Mass vs. profile shape ($1/n$). For the galaxies and galaxy clusters, the shape parameters n have come from the best-fitting Sérsic $R^{1/n}$ model to the (projected) luminosity and X-ray profiles, respectively. The galaxy stellar masses and cluster gas masses are shown here. For dark matter halos the virial masses are shown, and the shape parameters come from the best-fitting Prugniel-Simien model. (Note that the value of $1/n$ from the Prugniel-Simien model applied to a density profile is equivalent to the value of n from Sérsic’s model applied to the projected distribution.) We are plotting baryonic properties for the galaxies alongside dark matter properties for the simulated halos. *Filled stars*, N -body dark matter halos from this paper; *open plus signs*, galaxy clusters from Demarco et al. (2003); *dots*, dwarf elliptical (dE) galaxies from Binggeli & Jerjen (1998); *triangles*, dE galaxies from Stiavelli et al. (2001); *open stars*, dE galaxies from Graham & Guzmán (2003); *asterisks*, intermediate to bright elliptical galaxies from Caon et al. (1993) and D’Onofrio et al. (1994).

from the Prugniel-Simien model fit to the dark matter density. Dynamical masses from the Demarco et al. (2003) study of galaxy clusters are shown. We have also included the elliptical galaxy compilation in Graham & Guzmán (2003), converting their B -band luminosities into solar masses using a stellar mass-to-light ratio of 5.3 (Worthey 1994; for a 12 Gyr old single stellar population) and an absolute B -band magnitude for the Sun of 5.47 B -mag (Cox 2000). This approach ignores the contribution from dark matter in galaxies. However, given the uncertainties on how M_{tot}/L varies with L (e.g., Trujillo et al. 2004 and references therein) we prefer not to apply this correction, and note that the galaxy masses in Figure 15 only reflect the stellar mass.

Figure 15 suggests that the simulated galaxy-sized halos have a different shape parameter, i.e., a different mass distribution, from the simulated cluster-sized halos. The same conclusion was reached by Merritt et al. (2005), who studied a different sample of N -body halos. The sample of dwarf galaxy- and galaxy-sized halos from that paper had a mean (plus or minus a standard deviation)⁶ profile shape $n = 3.04 \pm 0.34$, while the cluster-sized halos had $n = 2.38 \pm 0.25$. We observe this same systematic difference in our N -body halos. Taking the profile shape n from the Prugniel-Simien model fits to the density profile (equivalent to the value of n obtained by fitting Sérsic’s $R^{1/n}$ model to the projected distribution), we find $n = 3.59 \pm 0.65$ for our cluster-sized halos and $n = 2.89 \pm 0.49$ for our galaxy-sized halos. A Student t -test,

⁶ We remind that the uncertainty on the mean is not equal to the standard deviation.

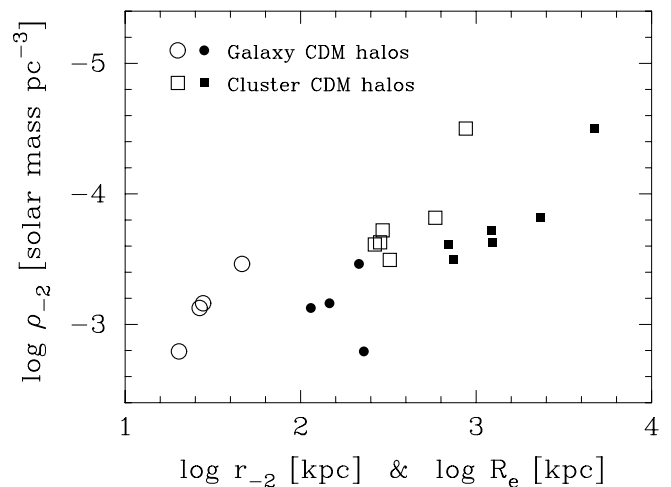


FIG. 16.—Density ρ_{-2} , where the logarithmic slope of the density profile equals -2 , plotted against (1) the radius where this occurs (*open symbols*) and (2) the effective radius (*filled symbols*) derived from the best-fitting Prugniel-Simien model (eq. [25]). Both ρ_{-2} and r_{-2} are also computed from the best-fitting Prugniel-Simien model (see Paper II). If a universal profile existed for these halos, the vertical difference would be constant for all halos.

without assuming equal variance in the two distributions, reveals that the above means are different at the 88% level. Applying the same test to the data set of Merritt et al. (2005, their Table 1, col. [2]), which is double the size of our sample and also contains dwarf galaxy-sized halos, we find that the means are different at the 99.98% level. We conclude that there is a significant mass dependence in the density profiles of simulated dark matter halos. Density profiles of more massive halos exhibit more curvature (smaller n) on a log-log plot.

The fact that n varies systematically with halo mass raises the question of which density scale and radial scale to use when characterizing halo structure. In the presence of a “universal” density profile, the ratio between R_e and r_{-2} (the radius where the logarithmic slope of the density profile equals -2 ; see Paper II) is a constant factor, but with varying values of n this is not the case. This remark also holds for the scale density, which is used to measure the contrast with the background density of the universe and provides the so-called halo concentration. This in turn raises the question of what “concentration” should actually be used, and whether systematic biases exist if one uses ρ_{-2} rather than, for instance, ρ_e . To reiterate this point: the density ratio between $r = r_{-2}$ and $r = R_e$ depends on the profile shape n , and thus, apparently, on the halo mass.

In Figure 16 we show how the use of r_{-2} and R_e produce slightly different results in the size-density diagram (e.g., Fig. 8 of Navarro et al. 2004). The relation between size (or equivalently mass) and central concentration (or density) varies depending on how one chooses to measure the sizes of the halos.

To better explore how the homology (i.e., universality) of CDM halos is broken, it would be beneficial to analyze a large, low-resolution sample of halos from a cosmological cube simulation in order to obtain good statistics. Moreover, the collective impact from differing degrees of virialization in the outer regions, possible debris wakes from larger structures, global ringing induced by the last major merger, triaxiality, and the presence of large subhalos could be quantified.

7. SUMMARY

We presented a nonparametric algorithm for extracting smooth and continuous representations of spherical density profiles from

N -body data and applied it to a sample of simulated dark matter halos. All halos exhibit a continuous variation of logarithmic density slope with radius; in the case of the Λ CDM halos, the variation of slope with radius is close to a power law. We then compared the ability of a variety of parametric models to reproduce the nonparametric $\rho(r)$ values. Over the fitted radial range $0.01 \lesssim r/r_{\text{vir}} < 1$, both the Einasto $r^{1/n}$ model (identical in functional form to Sérsic's model but expressed in terms of space, rather than projected, radius and density) and the Prugniel-Simien model (an analytical approximation to a deprojected Sérsic law) provide a better description of the data than the $(1, 3, \gamma)$ model, i.e., the NFW-like double-power-law model with inner slope γ . Moreover, unlike the $(1, 3, \gamma)$ model, both of these models have finite total mass and are also capable of describing the density profiles of halos formed from the cold collapse of a spherical overdensity (Fig. 6).

The single function that provides the best overall fit to the halo density profiles is Einasto's law, equation (20):

$$\rho(r) = \rho_e \exp\left\{-d_n \left[(r/r_e)^{1/n} - 1\right]\right\},$$

with d_n defined as in equation (24). This conclusion is consistent with that of an earlier study (Merritt et al. 2005) that was based on a different set of N -body halos. Typical values of the "shape" parameter n in equation (20) are $4 \lesssim n \lesssim 7$ (Table 1). Corresponding n -values from Sérsic profile fits to the projected (surface) density range from ~ 3 to ~ 3.5 (Fig. 15).

We propose that Einasto's model, equation (20), be more widely used to characterize the density profiles of N -body halos. As noted above, Einasto's model has already found application in a number of observationally motivated studies of the distribution of mass in galaxies and galaxy clusters. We propose also that the suitability of Einasto's model for describing the luminous density profiles of galaxies should be evaluated, either by projecting equation (20) onto the plane of the sky or by comparing equation (20) directly with deprojected luminosity profiles. Such a study could strengthen

the already strong connection between the density profiles of galaxies and N -body dark matter halos (Merritt et al. 2005).

While equation (20) is a good description of all of the halo models considered here, we found that systematic differences do exist in the best-fit models that describe N -body halos formed via hierarchical merging on the one hand, and those formed via spherical collapse on the other hand, in the sense that the latter have substantially smaller shape parameters, $n \approx 3.3$ (Table 1). That is, the density profiles in the cold-collapse halos decline more quickly than r^{-3} at large radii and have shallower inner profile slopes than those produced in simulations of hierarchical merging.

With regard to just the noncollapse models, we also found systematic differences between the cluster- and galaxy-sized halos. The latter are slightly better fitted by the three-parameter Dehnen-McLaughlin model, and the former are slightly better fitted by the Prugniel-Simien model (Table 4). This, together with the observation that more massive halos tend to have smaller shape parameters n (Fig. 15), suggests that there may not be a truly "universal" density profile that describes Λ CDM halos.

We kindly thank Gary Mamon for his detailed comments on this manuscript, as well as a second, anonymous referee. We are also grateful to Walter Dehnen and Dean McLaughlin for their helpful corrections and comments, and to Carlo Nipoti and Luca Ciotti. We also wish to thank Peeter Tenjes for tracking down and kindly faxing us copies of Einasto's original papers in Russian. A. G. acknowledges support from NASA grant HST-AR-09927.01-A from the Space Telescope Science Institute, and from the Australian Research Council through Discovery Project Grant DP0451426. D. M. was supported by grants AST 04-20920 and AST 04-37519 from the National Science Foundation and grant NNG 04GJ48G from NASA. J. D. is grateful for financial support from the Swiss National Science Foundation. B. T. acknowledges support from Department of Energy grant G1A62056.

REFERENCES

- Aarseth, S. J. 1963, *MNRAS*, 126, 223
 Abdelsalam, H. M., Saha, P., & Williams, L. L. R. 1998, *AJ*, 116, 1541
 Aceves, H., Velázquez, H., & Cruz, F. 2006, *MNRAS*, submitted (astro-ph/0601412)
 Aguilar, L. A., & Merritt, D. 1990, *ApJ*, 354, 33
 Austin, C. G., Williams, L. L. R., Barnes, E. I., Babul, A., & Dalcanton, J. J. 2005, *ApJ*, 634, 756
 Bertschinger, E. 1985, *ApJS*, 58, 39
 Binggeli, B., & Jerjen, H. 1998, *A&A*, 333, 17
 Binney, J. J. 1982, *MNRAS*, 200, 951
 Burkert, A. 1995, *ApJ*, 447, L25
 Caon, N., Capaccioli, M., & D'Onofrio, M. 1993, *MNRAS*, 265, 1013
 Cardone, V. F. 2004, *A&A*, 415, 839
 Cardone, V. F., Piedipalumbo, E., & Tortora, C. 2005, *MNRAS*, 358, 1325
 Carlberg, R. G., Lake, G., & Norman, C. A. 1986, *ApJ*, 300, L1
 Ciotti, L. 1991, *A&A*, 249, 99
 Cox, D. P. 2000, *Allen's Astrophysical Quantities* (New York: AIP)
 Cox, D. R., & Hinkley, D. V. 1974, *Theoretical Statistics* (London: Chapman & Hall)
 Davies, J. I., Phillipps, S., Cawson, M. G. M., Disney, M. J., & Kibblewhite, E. J. 1988, *MNRAS*, 232, 239
 Dehnen, W., & McLaughlin, D. E. 2005, *MNRAS*, 363, 1057
 Demarco, R., Magnard, F., Durret, F., & Márquez, I. 2003, *A&A*, 407, 437
 de Vaucouleurs, G. 1948, *Ann. d'Astrophys.*, 11, 247
 Diemand, J., Moore, B., & Stadel, J. 2004a, *MNRAS*, 352, 535
 ———. 2004b, *MNRAS*, 353, 624
 Diemand, J., Zemp, M., Moore, B., Stadel, J., & Carollo, C. M. 2005, *MNRAS*, 364, 665
 D'Onofrio, M., Capaccioli, M., & Caon, N. 1994, *MNRAS*, 271, 523
 Dubinski, J., & Carlberg, R. 1991, *ApJ*, 378, 496
 Durret, F., Lima Neto, G. H., & Forman, W. 2005, *A&A*, 432, 809
 Efstathiou, G. P., Frenk, C. S., White, S. D. M., & Davis, M. 1988, *MNRAS*, 235, 715
 Einasto, J. 1965, *Trudy Inst. Astrofiz. Alma-Ata*, 5, 87
 ———. 1968, *Tartu Astron. Obs. Publ.*, 36(5–6), 414
 ———. 1969, *Astrofizika*, 5, 137
 Einasto, J., & Haud, U. 1989, *A&A*, 223, 89
 Eke, V. R., Cole, S., & Frenk, C. S. 1996, *MNRAS*, 282, 263
 Fillmore, J. A., & Goldreich, P. 1984, *ApJ*, 281, 1
 Flores, R. A., & Primack, J. R. 1994, *ApJ*, 427, L1
 Frenk, C. S., White, S. D. M., Davis, M., & Efstathiou, G. P. 1988, *ApJ*, 327, 507
 Graham, A. W., & Colless, M. M. 1997, *MNRAS*, 287, 221
 Graham, A. W., & Driver, S. 2005, *Publ. Astron. Soc. Australia*, 22(2), 118 (astro-ph/0503176)
 Graham, A. W., Erwin, P., Trujillo, I., & Asensio Ramos, A. 2003, *AJ*, 125, 2951
 Graham, A. W., & Guzmán, R. 2003, *AJ*, 125, 2936
 Graham, A. W., Lauer, T., Colless, M. M., & Postman, M. 1996, *ApJ*, 465, 534
 Graham, A. W., Merritt, D., Moore, B., Diemand, J., & Terzić, B. 2006a, *AJ*, 133, 2701 (Paper II)
 ———. 2006b, *AJ*, 133, 2711 (Paper III)
 Graham, A. W., Trujillo, N., & Caon, N. 2001, *AJ*, 122, 1707
 Hénon, M. 1964, *Ann. d'Astrophys.*, 27, 83
 Hermquist, L. 1990, *ApJ*, 356, 359
 Hoffman, Y. 1988, *ApJ*, 328, 489
 Jaffe, W. 1983, *MNRAS*, 202, 995
 Jing, Y. P., & Suto, Y. 2000, *ApJ*, 529, L69
 Klypin, A., Kravtsov, A. V., Bullock, J. S., & Primack, J. R. 2001, *ApJ*, 554, 903

- Kravtsov, A. V., Klypin, A. A., Bullock, J. S., & Primack, J. R. 1998, *ApJ*, 502, 48
- Lima Neto, G. B., Gerbal, D., & Márquez, I. 1999, *MNRAS*, 309, 481
- Mamon, G. A., & Łokas, E. L. 2005, *MNRAS*, 362, 95
- Márquez, I., Lima Neto, G. B., Capelato, H., Durret, F., & Gerbal, D. 2000, *A&A*, 353, 873
- Márquez, I., Lima Neto, G. B., Capelato, H., Durret, F., Lanzoni, B., & Gerbal, D. 2001, *A&A*, 379, 767
- Mellier, Y., & Mathez, G. 1987, *A&A*, 175, 1
- Merritt, D. 1996, *AJ*, 111, 2462
- Merritt, D., & Aguilar, L. A. 1985, *MNRAS*, 217, 787
- Merritt, D., Navarro, J. F., Ludlow, A., & Jenkins, A. 2005, *ApJ*, 624, L85
- Merritt, D., Tremaine, S., & Johnstone, D. 1989, *MNRAS*, 236, 829
- Merritt, D., & Tremblay, B. 1994, *AJ*, 108, 514
- Miller, C. J., Nichol, R. C., Genovese, C., & Wasserman, L. 2002, *ApJ*, 565, L67
- Moore, B. 1994, *Nature*, 370, 629
- Moore, B., Governato, F., Quinn, T., Stadel, J., & Lake, G. 1998, *ApJ*, 499, L5
- Moore, B., Quinn, T., Governato, F., Stadel, J., & Lake, G. 1999, *MNRAS*, 310, 1147
- Navarro, J. F., Frenk, C. S., & White, S. D. M. 1995, *MNRAS*, 275, 720
- Navarro, J. F., et al. 2004, *MNRAS*, 349, 1039
- Nipoti, C., Londrillo, P., & Ciotti, L. 2006, *MNRAS*, 370, 681
- Peebles, P. J. E. 1970, *AJ*, 75, 13
- Pignatelli, E., & Galletta, G. 1999, *A&A*, 349, 369
- Poveda, A., Iturriaga, R., & Orozco, I. 1960, *Bol. Obs. Tonantzintla Tacubaya* 2, 20, 3
- Prada, F., Klypin, A. A., Simonneau, E., Betancort Rijo, J., Santiago, P., Gottlöber, S., & Sanchez-Conde, M. A. 2006, *ApJ*, 645, 1001
- Prugniel, P., & Simien, F. 1997, *A&A*, 321, 111
- Rasia, E., Tormen, G., & Moscardini, L. 2004, *MNRAS*, 351, 237
- Reed, D., et al. 2005, *MNRAS*, 357, 82
- Sarazin, C. L. 1980, *ApJ*, 236, 75
- Scott, D. W. 1992, *Multivariate Density Estimation* (New York: Wiley)
- Sérsic, J.-L. 1963, *Bol. Asoc. Argentina Astron.*, 6, 41
- . 1968, *Atlas de Galaxias Australes* (Cordoba: Univ. Cordoba)
- Silverman, B. W. 1986, *Density Estimation for Statistics and Data Analysis* (London: Chapman & Hall)
- Spergel, D. N., et al. 2003, *ApJS*, 148, 175
- Stadel, J. 2001, Ph.D. thesis, Univ. Washington
- Statler, T. S., & Diehl, S. 2005, *BAAS*, 207, 178.07
- Stepanas, P. G., & Saha, P. 1995, *MNRAS*, 272, L13
- Stiavelli, M., Miller, B. W., Ferguson, H. C., Mack, J., Whitmore, B. C., & Lotz, J. M. 2001, *AJ*, 121, 1385
- Tenjes, P., Haud, U., & Einasto, J. 1994, *A&A*, 286, 753
- Terzić, B., & Graham, A. W. 2005, *MNRAS*, 362, 197
- Trujillo, I., Burkert, A., & Bell, E. F. 2004, *ApJ*, 600, L39
- van Albada, G. B. 1961, *AJ*, 66, 590
- van Albada, T. S. 1982, *MNRAS*, 201, 939
- Wang, X., Woodroffe, M., Walker, M. G., Mateo, M., & Olszewski, E. 2005, *ApJ*, 626, 145
- West, M. J., Dekel, A., & Oemler, A., Jr. 1987, *ApJ*, 316, 1
- Worthey, G. 1994, *ApJS*, 95, 107
- Young, C. K., & Currie, M. J. 1995, *MNRAS*, 273, 1141
- Young, P. J. 1976, *AJ*, 81, 807
- Zhao, H. S. 1996, *MNRAS*, 278, 488

Note added in proof.—In the residual plots of Figures 5–9, 10, and 14, the quantity plotted in the vertical direction is minus what is stated in the axis labels.